Deterministic Reconfiguration of Flight Control Systems for Multirotor UAV Package Delivery

Anthony Gong
Aerospace Engineer
U.S. Army DEVCOM
Aviation & Missile Center
Moffett Field, CA, USA

Mark B. Tischler*
Senior Technologist
U.S. Army DEVCOM
Aviation & Missile Center
Moffett Field, CA, USA

Ronald A. Hess
Professor Emeritus
University of California, Davis
Davis, CA, USA

ABSTRACT

Multirotor UAS are prime candidates for autonomous package delivery due to their VTOL capability and payload-carrying capacity. The effect of payloads on flight control system performance is investigated for three different inner-loop flight control system architectures, namely, explicit model following, nonlinear dynamic inversion, and incremental nonlinear dynamic inversion. Outer-loop flight control systems are wrapped around the various inner-loop architectures for waypoint tracking control. The flight control systems are designed and optimized using CONDUIT® to meet a common, comprehensive set of stability and performance specifications. Deterministic reconfiguration was designed for each inner-loop control architecture to account for the change in vehicle dynamics when a payload is added or removed. Robustness analyses are conducted considering both deterministic payload variations and modeling uncertainty. A notional package delivery mission scenario is simulated using a full-flight envelope stitched model with measurement noise and turbulence models identified from flight test data. The mission scenario is simulated for three different cases to evaluate the baseline performance, the degraded performance when a payload is added, and the recovery of performance with deterministic reconfiguration of the flight control systems.

INTRODUCTION

The mechanical simplicity, cost, and versatility of multirotor unmanned aerial vehicles (UAVs) have contributed to their increasing use and consideration in numerous industries. Their vertical takeoff and landing (VTOL) capability allows for low-speed precision maneuvering in urban environments without the need for a runway and ability to carry payloads (e.g. cameras, sensor payloads, etc.) make them an ideal candidate for use in package delivery. They are currently evaluated for package delivery in commercial applications (e.g. Amazon, UPS, DHL). Figure 1 shows examples of multirotor UAS used for food and medicine delivery and tactical resupply. Payloads will affect the bare-airframe dynamics of the aircraft and the closed-loop performance of the flight control system (FCS), so accurate models are required to design, assess, and evaluate appropriate flight control systems to ensure safety of flight for a wide range of payloads.

A wide range of flight control strategies have been utilized on multirotor UAVs to improve performance and robustness. Online adaptive methods have been utilized to identify changes to the vehicle for small payloads (Ref. 1) or aircraft damage (Ref. 2) and adapt the control system accordingly. Smeur et al. showed that incremental nonlinear dynamic inversion (INDI) is robust to the presence of a small payload (Ref. 3) and also used online adaptive control in conjunction with INDI (Ref. 4) on a small quadrotor UAV.

As opposed to methods that utilize online, nondeterministic, adaptation, *deterministic reconfiguration* of the flight control system (i.e. updating or reconfiguring flight control system parameters such as feedback gains or onboard models for known changes/variations) is well suited for package delivery with UAVs since payload mass properties (mass, inertia, center of gravity) are *measureable* quantities rather than unknown uncertainties. Since the simulation and control system updates are deterministic, this approach will provide for repeatable flight dynamics characteristics without online adaptation and allow a simpler path to DoD/FAA certification. Gain scheduling is an example of such deterministic offline adaptation commonly used to account for change in aircraft dynamics with parameters such as airspeed (Ref. 5). Feedback linearization techniques such as nonlinear dynamic inversion (NDI) or INDI can also be leveraged to deterministically reconfigure the FCS by updating the onboard model such that is it representative of the vehicle dynamics with the known payload.

This paper investigates the effects of payloads multirotor flight control system performance and is an extension of the work found in (Ref. 6). It first presents the full-flight envelope simulation "stitched" model (Ref. 7) of the custom-built mul-

*Retired from U.S. Army; currently, Tischler Aeronautics

Presented at the Vertical Flight Society's 77th Annual Forum & Technology Display (virtual), May 11–13, 2021.

(a) Ele.me food delivery drone (Shanghai)

(b) DHL Parcelcopter (Tanzania)

(c) SURVICE TRV-150 (Tactical Resupply Vehicle)

Figure 1: Multirotors used for package delivery.

tirotor package delivery vehicle (Ref. 8). Then, it presents flight test data from a loaded configuration motivating the need for FCS reconfiguration. Next, three distinct flight control system architectures, namely, explicit model following, nonlinear dynamic inversion, and incremental nonlinear dynamic inversion are described in brief detail. This is followed by the optimization methodology, results, and a discussion of each architecture's reconfiguration strategy. Simulation case studies of a notional package delivery mission scenario with and without reconfiguration are shown. A comprehensive robustness analyses of the flight control system to uncertainties is described and the paper finished with conclusions.

VEHICLE AND FLIGHT DYNAMICS MODEL DESCRIPTION

The flight vehicle used in this study is a custom-built octocopter designed to serve as a generic package delivery vehicle (Figure 2). The octocopter has a weight of 18.0 pounds, a motor-to-motor distance of 4.2 feet, thrust-to-weight ratio of 3.6, maximum effective payload of 40 pounds, and a hovering flight time of 20 minutes. It was modified to carry a large, custom-designed, cargo bay (24.0 in x 24.0 in x 11.0 in) built with a carbon fiber internal structure for rigidity and encased in foam to form the exterior. The cargo bay allows for a wide range of internal payloads while keeping the aerodynamic characteristics of the aircraft constant throughout flight tests with varying loading configurations.

Figure 2: Octocopter equipped with a large cargo bay.

Accurate linear models of the vehicle (without an internal payload) were obtained from system identification (Ref. 8) at hover, 10-knot, and 20-knot flight conditions. These models served as anchor points in a model stitching architecture (Ref. 9) to produce a continuous, full-flight envelope simulation model capable of accurately extrapolating to off-nominal loading conditions such as those with a payload (Ref. 7). This stitched model is a key enabling technology that allows for deterministic reconfiguration by accurately generating linear models of any payload configuration for the design and reconfiguration of flight control systems.

FLIGHT TESTS - LOADED CONFIGURATION

The vehicle was flight tested in two configurations to develop the stitched model: unloaded (empty cargo bay) and loaded (11.7-pound payload located in the corner of the cargo bay). The loaded configuration represents a case where the package is not located in the center of the cargo bay and the package's position bay shifts the center-of-gravity (CG) of the aircraft away from the geometric center in the direction of the payload.

A stock flight control system in Ardupilot, *Stabilize mode*, was used to flight test both loading configurations at 0, 10,

and 20 knots. The FCS was able to maintain stability of the aircraft, but not without undesirable response characteristics. Due to the heave command on take-off, rather than climbing into the air vertically, the offset CG coupled with a control system that is not configured for such a loading scenario caused the vehicle to dip forward and towards the right.

Figure 3 shows a time history of a thrust axis sweep in hover for the offset loaded configuration. Since the thrust axis is flown open-loop in *Stabilize mode*, the automated sweep summed into the pilot command is the same command at the input to the mixer. The offset CG causes undesirable coupling between the heave and lateral/longitudinal axes (i.e. heave command induce pitch and roll motions through the off-axis control derivative terms L_{thr} and M_{thr}. During a thrust-axis sweep, due to the payload-induced heave coupling, both the lateral and longitudinal axes mixer commands are shown to be correlated to the commanded thrust-axis sweep, particularly evident in the mid-frequency range between 15-25 seconds, while trying to regulate the uncommanded pitch and roll rate responsesAdditionally, the corner-loaded payload's effect can be seen in the nonzero trim controls (-16% and +7%) held by the lateral and longitudinal axes control systems (seen between 30-35 seconds) to maintain zero pitch and roll attitude in hover. This demonstrates the need for reconfiguration in the presence of a load in order to prevent undesirable off-axis responses.

FLIGHT CONTROL SYSTEMS

The inner and outer loops of three flight control systems were designed to evaluate their relative advantages and disadvantages in performance. The inner-loops regulate angular rates and attitudes while the outer-loops control vehicle velocity and position. The inner-loops utilized one of three strategies: explicit model following (EMF) (Ref. 10), nonlinear dynamic inversion (NDI) (Ref. 11), and incremental nonlinear dynamic inversion (INDI) (Ref. 12). The outer-loops utilized a classical PID-type feedback architecture. Figure 4 shows a schematic of the flight control systems.

The FCS inner-loop architectures, shown in Figure 5, have three common components: command models, commands delays, and feedback.

The command models are first or second order transfer functions containing parameters defining the desired response characteristics and response type to piloted or outer-loop commands. The command models are the same for all three FCS and constant throughout the three flight conditions. Equations 1 and 2 show the form for the command models, and Table 1 lists the parameter values used. The pitch and roll axes both have attitude-command/attitude-hold (ACAH) response types while the thrust axis is rate-command/height-hold (RCHH), and yaw axis is rate-command/direction-hold (RCDH).

$$\frac{\phi_{cmd}}{\delta_{lat_p}} = \frac{\theta_{cmd}}{\delta_{lon_p}} = \frac{K\omega_n^2}{s^2 + 2\zeta\omega_n s + \omega_n^2} \tag{1}$$

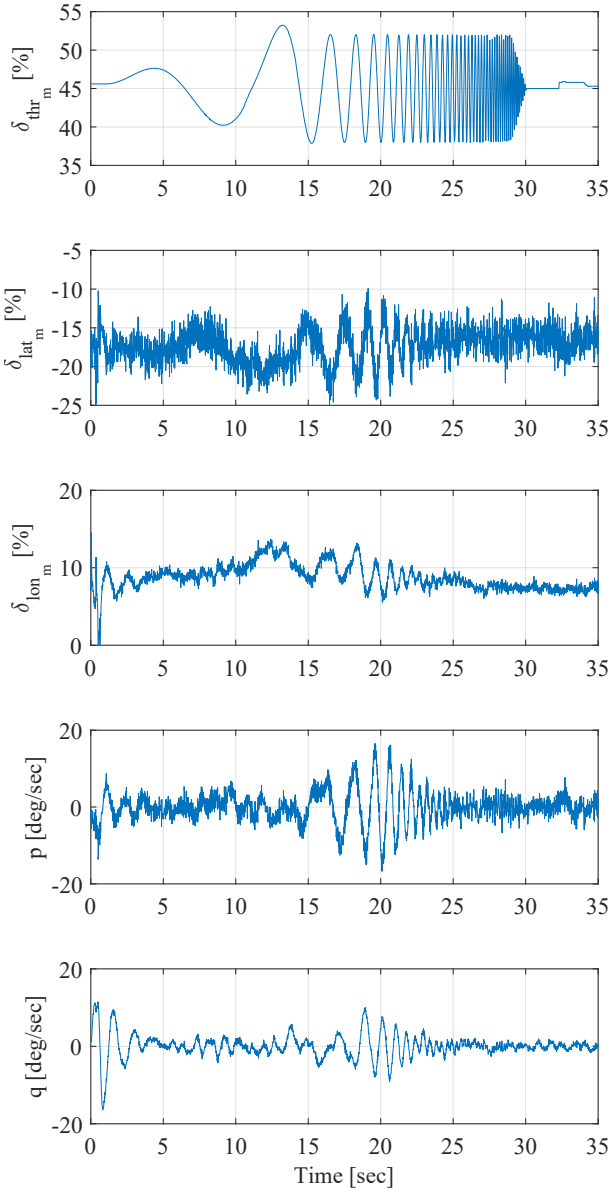

Figure 3: Thrust axis sweep in Ardupilot "Stabilize" mode of the loaded configuration in hover.

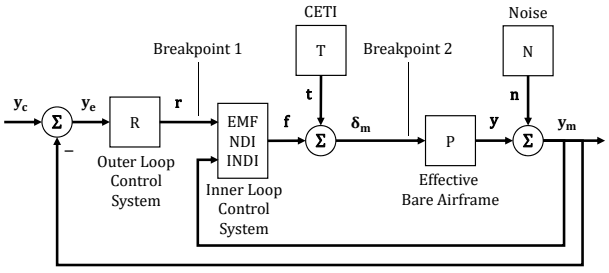

Figure 4: Flight control system architecture overview (lateral axis example).

$$\frac{\dot{h}_{cmd}}{\delta_{lat}} = \frac{r_{cmd}}{\delta_{yaw}} = \frac{K}{\tau s + 1} \tag{2}$$

Command delays are used to synchronize the signals commanded by the command models and sensor outputs. This

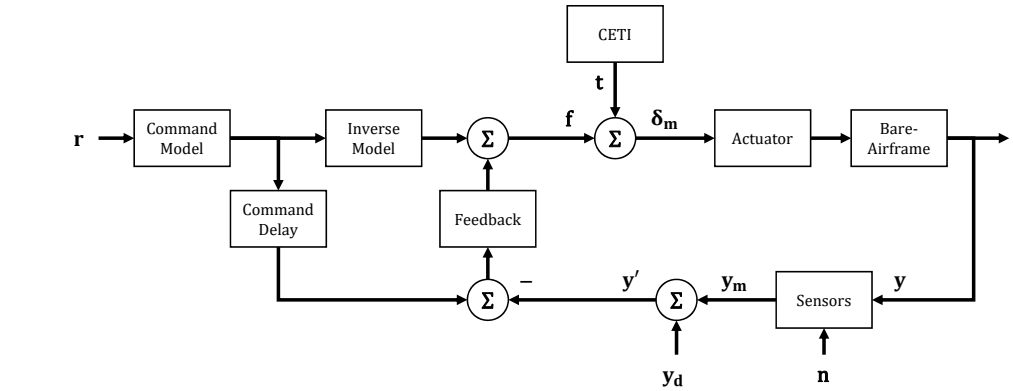

(a) Explicit model following (EMF) architecture.

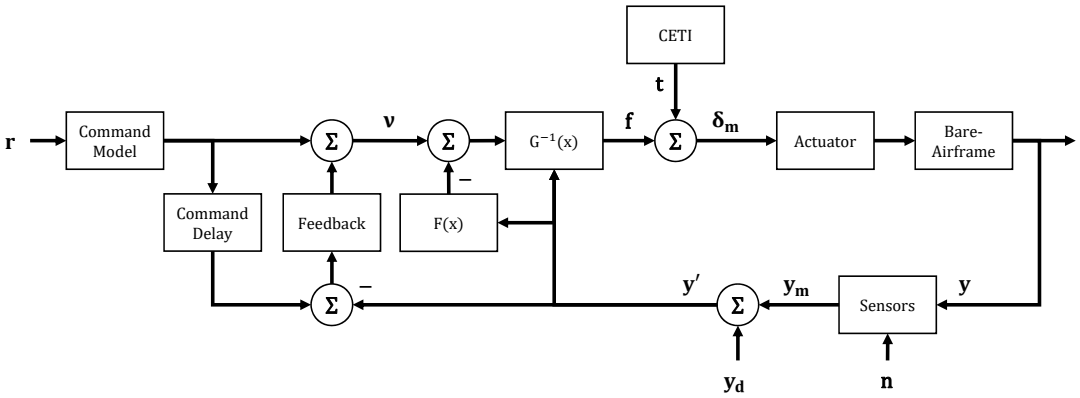

(b) Nonlinear dynamic inversion (NDI) architecture.

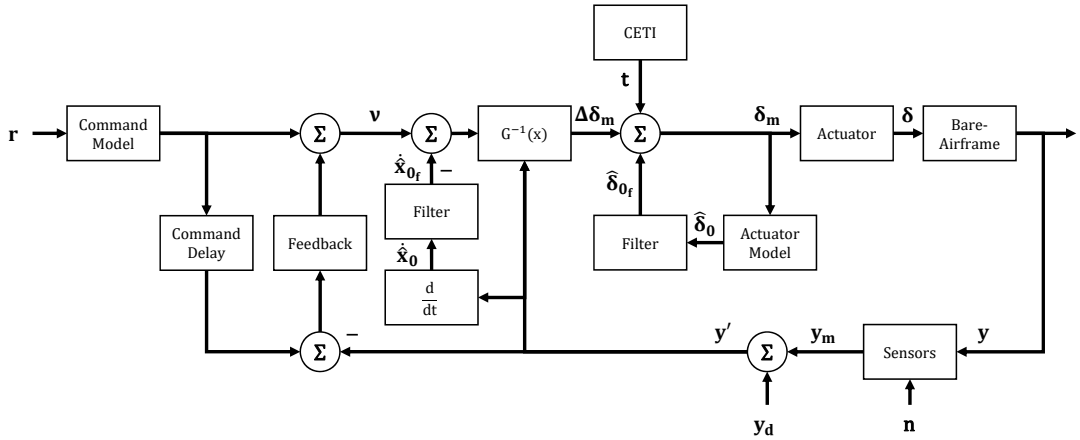

(c) Incremental nonlinear dynamic inversion (INDI) architecture.

Figure 5: Inner-loop flight control system architectures.

Table 1: Command model parameters and response types

Axis	Response Type	K	τ	ω_n	ζ
Lateral	ACAH	45	—	8	1.0
Longitudinal	ACAH	45	—	8	1.0
Thrust	RCHH	10	1.0	—	—
Yaw	RCDH	45	1.0	—	—

prevents over-driving the actuators without additional closed-loop phase delay (Ref. 13). Higher-order dynamics, sensor delays, and computational delays that are not accounted for by the inverse models are accounted for by the equivalent delay.

Figure 6 shows an example of the inner-loop feedback architecture which utilizes rate, attitude, attitude-integral, and lead-lag compensators on each axis. The feedback gains and lead-lag compensators are optimized by CONDUIT® to meet a comprehensive set of specifications. The attitude-integral gains are not optimized, but rather, constrained to 1/5 of the crossover frequency of that given axis to prevent excessive phase margin degradation (Refs. 9, 10). There is also a first-order low-pass filter on each axis fixed at 50 rad/sec to reject

high-frequency noise in the feedback path. The filter cutoff frequency was chosen to be 5 times the optimized inner-loop crossover frequency ($\omega_c = 10\ \frac{\text{rad}}{\text{sec}}$) from previous disturbance rejection research (Ref. 14). This ensures that this filter attenuates high frequency noise with minimal impact on the feedback control design and optimization.

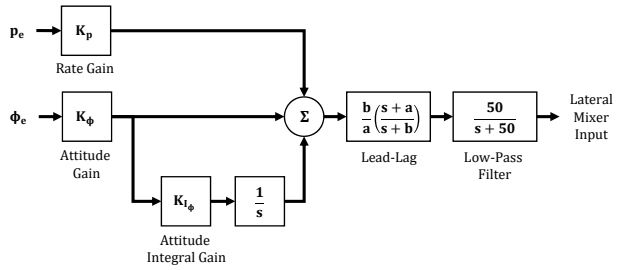

Figure 6: Inner-loop roll axis feedback structure.

Explicit Model Following

The EMF architecture, shown in Figure 5a, is a commonly used in rotorcraft flight control systems (Refs. 10, 15). It serves as a baseline to provide reference for the performance of a linear control system.

The inverse models are the reciprical of lower-order SISO model fits of the bare-airframe on-axis responses. Equations 3 (Ref. 16) and 4 show examples of how the lateral and yaw axes feed-forward the control inputs necessary to generate the command model response. Note that the inverse models are integrated with the command models to ensure an overall causal system (Ref. 9).

$$\delta_{lat_{ff}} = \frac{\ddot{\phi}_{cmd} - L_v \frac{g}{s - Y_v}\phi_{cmd}}{L_{lat}} \tag{3}$$

$$\delta_{yaw_{ff}} = \frac{\dot{r}_{cmd} - N_r r_{cmd}}{N_{\delta_{yaw}}} \tag{4}$$

Nonlinear Dynamic Inversion

Nonlinear dynamic inversion, shown in Figure 5b, is a feedback linearization technique that uses onboard models of the aircraft dynamics to cancel out the bare-airframe dynamics and render the vehicle dynamics as integrators from the perspective of the virtual input to the controlled variable. This flight control system architecture has been successfully used in the Joint Strike Fighter (JSF) program (Ref. 17).

Starting with control-affine nonlinear equations of the bare-airframe dynamics,

$$\dot{\boldsymbol{x}} = \boldsymbol{f}(\boldsymbol{x}) + \boldsymbol{g}(\boldsymbol{x})\boldsymbol{\delta} \tag{5}$$

$$\boldsymbol{y} = \boldsymbol{h}(\boldsymbol{x}) \tag{6}$$

where, $\boldsymbol{x}$ are the 6-DOF rigid-body states composed of the body-axis translational velocities $[u, v, w]$, the body-axis angular velocities $[p, q, r]$, and the Euler angles $[\phi, \theta, \psi]$.

$$\boldsymbol{x} = \begin{bmatrix} u & v & w & p & q & r & \phi & \theta & \psi \end{bmatrix}^{\mathrm{T}} \tag{7}$$

$\boldsymbol{\delta}$ are the four controls (lateral, longitudinal, thrust, yaw) at the input to the mixer.

$$\boldsymbol{\delta} = \begin{bmatrix} \delta_{lat} & \delta_{lon} & \delta_{thr} & \delta_{yaw} \end{bmatrix}^{\mathrm{T}} \tag{8}$$

The controlled variables, $\boldsymbol{y}$, are selected to be the body-axis angular velocities (p, q, r) and climb rate ($\dot{h}$) for stable zero dynamics. This retains a square system (4 inputs, 4 outputs) that includes the heave-axis within the inner-loop control system.

$$\boldsymbol{y} = \begin{bmatrix} p & q & r & \dot{h} \end{bmatrix}^{\mathrm{T}} \tag{9}$$

Taking the derivative of Eq. 6,

$$\dot{\boldsymbol{y}} = \frac{\partial \boldsymbol{h}(\boldsymbol{x})}{\partial \boldsymbol{x}}\dot{\boldsymbol{x}} = \boldsymbol{h}_{\boldsymbol{x}}\dot{\boldsymbol{x}} = \boldsymbol{h}_{\boldsymbol{x}}\boldsymbol{f}(\boldsymbol{x}) + \boldsymbol{h}_{\boldsymbol{x}}\boldsymbol{g}(\boldsymbol{x})\boldsymbol{\delta} \tag{10}$$

Defining $\boldsymbol{F}(\boldsymbol{x}) = \boldsymbol{h}_{\boldsymbol{x}}\boldsymbol{f}(\boldsymbol{x})$ and $\boldsymbol{G}(\boldsymbol{x}) = \boldsymbol{h}_{\boldsymbol{x}}\boldsymbol{g}(\boldsymbol{x})$,

$$\dot{\boldsymbol{y}} = \boldsymbol{F}(\boldsymbol{x}) + \boldsymbol{G}(\boldsymbol{x})\boldsymbol{\delta} \tag{11}$$

The partial derivative of the output function with respect to the states, $\boldsymbol{h}_{\boldsymbol{x}}$, is shown in matrix form:

$$\begin{aligned} \boldsymbol{h}_{\boldsymbol{x}} &= \frac{\partial \boldsymbol{h}(\boldsymbol{x})}{\partial \boldsymbol{x}} \\ &= \begin{bmatrix} \frac{\partial p}{\partial x} & \frac{\partial q}{\partial x} & \frac{\partial h}{\partial x} & \frac{\partial r}{\partial x} \end{bmatrix}^{\mathrm{T}} \\ &= \begin{bmatrix} 0 & 0 & 0 & 1 & 0 & 0 & 0 & 0 & 0 \\ 0 & 0 & 0 & 0 & 1 & 0 & 0 & 0 & 0 \\ \frac{\partial \dot{h}}{\partial u} & \frac{\partial \dot{h}}{\partial v} & \frac{\partial \dot{h}}{\partial w} & 0 & 0 & 0 & \frac{\partial \dot{h}}{\partial \phi} & \frac{\partial \dot{h}}{\partial \theta} & 0 \\ 0 & 0 & 0 & 0 & 0 & 1 & 0 & 0 & 0 \end{bmatrix} \end{aligned} \tag{12}$$

where:

$$\begin{aligned} \frac{\partial \dot{h}}{\partial u} &= sin(\theta) \\ \frac{\partial \dot{h}}{\partial v} &= -sin(\phi)cos(\theta) \\ \frac{\partial \dot{h}}{\partial w} &= -cos(\phi)cos(\theta) \\ \frac{\partial \dot{h}}{\partial \phi} &= -V\ cos(\phi)cos(\theta) + W\ sin(\phi)cos(\theta)\ ) \\ \frac{\partial \dot{h}}{\partial \theta} &= U\ cos(\theta) + V\ sin(\phi)sin(\theta) + W\ cos(\phi)sin(\theta) \end{aligned} \tag{13}$$

The nonlinear functions, $\boldsymbol{f}(\boldsymbol{x})$, are used to compute forces and moments due to state aerodynamics, gravity, and Coriolis (denoted in Eq. 14 with subscript *a*) *without* contributions from

control inputs. Specifically, the gravity and Coriolis terms are nonlinear reconstructions from the sensed states whereas the forces/moments from aerodynamics are calculated from lookup tables of the stability derivatives.

$$\begin{aligned}\boldsymbol{F}(\boldsymbol{x}) &= \boldsymbol{h_x}\begin{bmatrix}\dot{u}_a & \dot{v}_a & \dot{w}_a & \dot{p}_a & \dot{q}_a & \dot{r}_a & \dot{\phi}_a & \dot{\theta}_a & \dot{\psi}_a\end{bmatrix}^{\mathrm{T}} \\ &= \begin{bmatrix} \dot{p}_a \\ \dot{q}_a \\ \frac{\partial \dot{h}}{\partial u}\dot{u}_a + \frac{\partial \dot{h}}{\partial v}\dot{v}_a + \frac{\partial \dot{h}}{\partial w}\dot{w}_a + \frac{\partial \dot{h}}{\partial \phi}\dot{\phi}_a + \frac{\partial \dot{h}}{\partial \theta}\dot{\theta}_a \\ \dot{r}_a \end{bmatrix}\end{aligned} \tag{14}$$

The control effectiveness matrix, $\boldsymbol{G^{-1}(x)}$, is computed from the nonlinear output function $\boldsymbol{h_x}$ and the control derivatives matrix. In this case, $\boldsymbol{g(x) = B(x) = B}(u)$, where the control derivatives are a function of airspeed, u.

$$\boldsymbol{G(x)} = \boldsymbol{h_x}\begin{bmatrix} X_{lat} & X_{lon} & X_{thr} & X_{yaw} \\ Y_{lat} & Y_{lon} & Y_{thr} & Y_{yaw} \\ Z_{lat} & Z_{lon} & Z_{thr} & Z_{yaw} \\ L_{lat} & L_{lon} & L_{thr} & L_{yaw} \\ M_{lat} & M_{lon} & M_{thr} & M_{yaw} \\ N_{lat} & N_{lon} & N_{thr} & N_{yaw} \\ 0 & 0 & 0 & 0 \\ 0 & 0 & 0 & 0 \\ 0 & 0 & 0 & 0 \end{bmatrix} \tag{15}$$

With the exception of the on-axis control derivatives and the CG-offset induced cross-coupling derivatives (L_{thr} and M_{thr}), all other terms in Eq. 15 are zero, and effectively reduces to Eq. 16.

$$\boldsymbol{G(x)} = \begin{bmatrix} L_{lat} & 0 & L_{thr} & 0 \\ 0 & M_{lon} & M_{thr} & 0 \\ 0 & 0 & \frac{\partial \dot{h}}{\partial w} Z_{thr} & 0 \\ 0 & 0 & 0 & N_{yaw} \end{bmatrix} \tag{16}$$

Given perfect models, inversion of $\boldsymbol{G(x)}$ directly cancels the payload-induced cross-coupling dynamics.

Incremental Nonlinear Dynamic Inversion

Incremental nonlinear dynamic inversion, shown in Figure 5c, is a technique developed to overcome the robustness issues of nonlinear dynamic inversion that comes from the requirement of accurately reconstructing Eq. 14. The main advantage of INDI is that the reliance is instead replaced by directly estimating or sensing the derivative of the controlled variable. This is accomplished by either sensing or feeding back an estimate of the command from the previous time step and computing an incremental change in the input, $\boldsymbol{\Delta\delta}$. A brief derivation of the INDI formulation is presented here.

Starting with a set of nonlinear equations of motion,

$$\boldsymbol{\dot{x} = f(x, \delta)} \tag{17}$$

Linearize about the current operating point, subscript 0,

$$\begin{aligned}\boldsymbol{\dot{x}} &\approx \boldsymbol{f(x_0, \delta_0)} + \boldsymbol{\frac{\partial f(x,\delta)}{\partial x}\Big|_{x_0,\delta_0}(x - x_0)} + \boldsymbol{\frac{\partial f(x,\delta)}{\partial \delta}\Big|_{x_0,\delta_0}(\delta - \delta_0)} \\ &\approx \boldsymbol{\dot{x}_0 + F(x_0, \delta_0)\Delta x + G(x_0, \delta_0)\Delta\delta}\end{aligned} \tag{18}$$

Assuming that the change in states is much slower than the change due to control (i.e. $\boldsymbol{F(x_0, \delta_0)\Delta x \ll G(x_0, \delta_0)\Delta\delta}$), which is valid for small time steps, then,

$$\boldsymbol{\dot{x} \approx \dot{x}_0 + G(x_0, \delta_0)\Delta\delta} \tag{19}$$

To develop a control law for which the nonlinear system is rendered a simple integrator, $\frac{y}{v} = \frac{1}{s}$,

$$\boldsymbol{\Delta\delta \approx G^{-1}(x_0, \delta_0)(\nu - \dot{x}_0)} \tag{20}$$

Actuator Model The actuator output, propeller revolutions per minute (RPM), is not typically sensed in multirotor UAV, so the actuator model is used in the INDI flight control system. The actuator model was identified from from flight test data and independently validated using thrust stand measurements (Ref. 8). Non-dimensional mixer inputs are converted to pulse-width-modulation (PWM) where the actuator model (Eq. 21) is implemented with position and rate limits, and then converted back to non-dimensional units for proper bounding of the actuator with known physical PWM range constraints of 1000-2000.

$$\frac{\hat{\delta}}{\delta_m}(s) = \frac{\omega_{lag}}{s + \omega_{lag}} = \frac{18.9}{s + 18.9} \tag{21}$$

Filters The INDI architecture requires the sensed or estimated derivatives of the controlled variables: $[\dot{p}, \dot{q}, \dot{r}, \ddot{h}]$. A common method is to differentiate the angular velocity and altitude-rate signals. A second-order low-pass filter (Eq. 22) is designed to attenuate the high frequency noise that would otherwise be fed back into the system due to differentiation.

$$H(s) = \frac{\omega_n^2}{s^2 + 2\zeta\omega_n s + \omega_n^2} = \frac{60^2}{s^2 + 2 * 0.5 * 60s + 60^2} \tag{22}$$

A parametric set of filter designs with damping ratios ranging from 0.5 to 1.0 and natural frequencies from 20 to 60 rad/sec were tested on the differentiated flight test data. Figure 7 shows the roll acceleration signal differentiated from the roll rate flight data and the filter design (ζ = 0.5, ω_n = 60 rad/sec) selected for use in this paper.

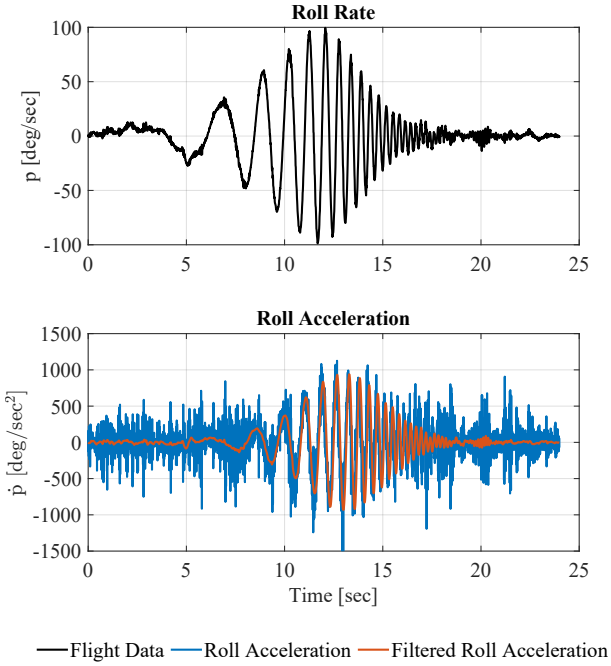

Figure 7: Roll acceleration from differentiated roll rate before and after low-pass filter.

FLIGHT CONTROL SYSTEM OPTIMIZATION

The three flight control systems were optimized to meet a common set of specifications using the Control Designers Unified Interface (CONDUIT®) with the details of the design process given in (Ref. 10). The design procedure is summarized herein. Tables 2 and 3 show the specifications used to optimize the inner and outer loops, respectively. Inner-loop and outer-loop feedback gains were optimized at 0, 10, and 20-knots for each flight control system.

Method

The inner-loops design parameters (feedback gains) were first optimized to the set of specifications shown in Table 2. The inner loop was designed to meet a more stringent (10% increased) stability margin requirement in anticipation of the subsequent degradation expected from the closure of the outer-loops. A design margin optimization (DMO) was performed on the crossover frequency and disturbance rejection bandwidth (DRB) specifications on all four axes in which the two requirements were incrementally increased to maximize performance. The lead-lag filter on each axis is parameterized based on the frequency of maximum added phase, ω_{LL}, and the amount of phase added, ϕ_{LL}. ω_{LL} is tied to the Level 1/2 crossover frequency boundary such that the lead-lag filter's maximum added phase occurs at crossover while ϕ_{LL} is a design parameter optimized by CONDUIT®. The LlpMnG1 specification is used as a summed objective to minimize the amount of added phase to limit amplification of high frequency noise.

The outer-loops feedback gains are optimized to the specifications in Table 3 after closure of the inner-loops and keeping the inner-loop design parameters constant. Stability margins during this phase of optimization are evaluated at two places as seen in Figure 4.

1. At the input to the inner-loop
2. At the input to the actuators

The latter prevents excessive degradation of stability margins at the actuator while optimizing outer-loop design parameters. As such, the 10% extra margin built in during the design of the inner-loops provides "headroom" for the design of the outer loop feedback gains (Ref. 10).

Results

The closure of the inner feedback loops effectively transforms the bare-airframe into an actuator with characteristics defined by the command models. Therefore, the focus here is to investigate the outer-loop performance which determines how well each control system is able to track waypoint commands and reject position and velocity disturbances.

Figure 8 shows the two specifications for which design margin optimization was performed on the outer-loop to maximize performance: crossover frequency and disturbance rejection bandwidth. The EMF and NDI control systems optimized to similar outer-loop crossover frequencies across all outer-loop axes while the INDI control system achieved noticeably lower results. The same trends are less pronounced in DRB, but INDI consistently had the lowest value for all axes indicating lower outer-loop position disturbance rejection performance when compared to EMF and NDI.

The lower optimized performance (ω_c, DRB) of INDI across all axes is due to a lack of available robust stability margin broken at the actuator. Figure 9 shows the optimized broken-loop responses at the actuator on a Nichols plot after inner and outer loop optimization for the lateral axis. After the inner-loop has been optimized, it shows that all FCS satisfy the robust stability requirement by avoiding the exclusion zone. Notably, there is a significant amount of gain and phase buffer between the inner-loop response and the exclusion zone for EMF and NDI which demonstrates their robust stability. Comparatively, the INDI response wraps around the exclusion zone much more tightly, indicating that it is not nearly as robust in terms of stability when compared to EMF and NDI.

Since the NicMgG1 specification (broken at the actuator) is also imposed during outer-loop optimization, the design space for outer-loop feedback gains is limited by how much the inner-loop response can degrade towards to the Level 1/2 boundary of the exclusion zone. There is very little gain and phase left for INDI, so outer-loop optimization is limited to the extra buffer built in by using the 10% increased stability specification (NicMgG2) during inner-loop optimization. The outer-loop optimization is clearly bounded by NicMgG1

Table 2: Inner-Loop Control System Optimization Specifications.

Constraint Type	CONDUIT® Specification	Description
Hard Constraints	EigLcG1	Closed-loop eigenvalues in L.H.P.
	StbMgG2	10% increased Gain and Phase Margin broken at breakpoint 2
	NicMgG2	10% increased Nichols Margins broken at breakpoint 2
Soft Constraints	CrsMnG2	Minimum crossover frequency
	DstBwG1	Disturbance rejection bandwidth
	DstPkG1	Disturbance rejection peak
	ModFoG2	Command model following cost
	OlpOpG1	Open Loop Onset Point, command input
	OlpOpG2	Open Loop Onset Point, disturbance input
Summed Objectives	CrsLnG1	Minimize crossover frequency
	RmsAcG1	Minimize actuator RMS
	LlpMnG1	Minimize phase added by lead-lag filter

Table 3: Outer-Loop Control System Optimization Specifications.

Constraint Type	CONDUIT® Specification	Description
Hard Constraints	EigLcG1	Closed-loop eigenvalues in L.H.P.
	StbMgG1	Gain and Phase Margin broken at breakpoint 1
	NicMgG1	Nichols Margins broken at breakpoint 1
	StbMgG1	Gain and Phase Margin broken at breakpoint 2
	NicMgG1	Nichols Margins broken at breakpoint 2
Soft Constraints	CrsMnG2	Minimum crossover frequency
	DstBwG1	Disturbance rejection bandwidth
	DstPkG1	Disturbance rejection peak
Summed Objectives	CrsLnG1	Minimize crossover frequency
	RmsAcG1	Minimize actuator RMS
	LlpMnG1	Minimize phase added by lead-lag filter

specification broken at the actuator since all three FCS designs optimize to the edge of the Level 1/2 boundary of the exclusion zone.

DETERMINISTIC RECONFIGURATION

Deterministic reconfiguration is accomplished for the various FCS in different ways. The EMF FCS is reconfigured by updating the inverse model parameters and the inclusion of a cross-feed matrix $\boldsymbol{K_{cf}}$. The cross-feed matrix is computed using Eq. 23 via the pseudo-inverse of the control matrix for the loaded configuration, $\boldsymbol{B_L}$, and the control matrix of the nominal (unloaded) configuration, $\boldsymbol{B_N}$. It is designed to cancel off-axis heave-coupling derivatives due to the offset CG induced by the payload and maintain similar levels of performance as the optimized unloaded configuration (Ref. 10).

$$\boldsymbol{K_{cf} = B_L^{-1} B_N} \tag{23}$$

Reconfiguration of the feedback linearization based FCS is done by updating their respective onboard models. For NDI, $\boldsymbol{F(x)}$ and $\boldsymbol{G(x)}$ are updated with the mass, moments of inertia, and lookup tables containing stability derivatives, control derivatives, and trim states of the load configuration. For INDI, only the control effectiveness matrix, $\boldsymbol{G(x)}$, needs to be updated since it contains lookup tables of control derivatives.

FULL-FLIGHT ENVELOPE SIMULATION

The simulated mission is a notional package delivery route shown in Fig. 10. This route was designed to exercise the entire airspeed envelope from hover/low-speed vertical climbs to 20-knot cruise flight at altitude. This involved simulation using the nonlinear, continuous, full-flight envelope stitched model described in (Ref. 8), measurement noise simulated throughout the flight path, turbulence from Control Equivalent Turbulence Input (CETI) models, and the optimized feedback gains scheduled with low-pass filtered airspeed.

Control Equivalent Turbulent Input (CETI) Models

Lateral, longitudinal, and thrust axis Control Equivalent Turbulence Input (CETI) models were identified for the octocopter in previous research (Ref. 14). These models are used to produce realistic, simulated turbulence for evaluating how well each FCS can track waypoints in the presence of disturbances. The CETI models (Figure 5) generate control inputs that cause the model to respond as if flying in turbulence that was previously measured in flight. CETI models were identified at hover/low-speed regimes, so they were only active during the vertical climb/descent phases of this mission (path 1 and 5).

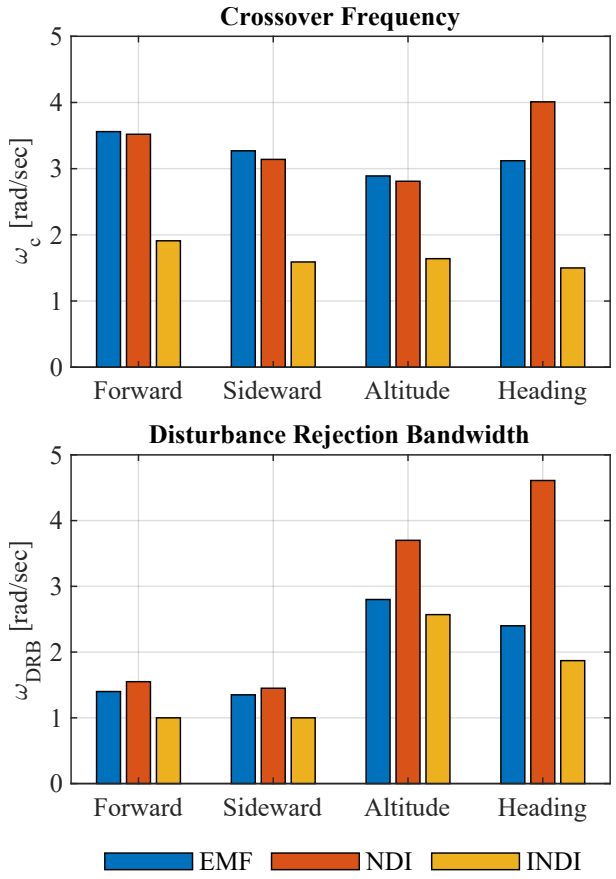

Figure 8: Optimized outer-loop crossover frequency and disturbance rejection bandwidth at hover.

Measurement Noise

Measurement noise models were identified from frequency sweep flight test data. During a frequency sweep for a given axis (e.g. longitudinal), due to the decoupled dynamics of the bare-airframe and the closed-loop flight control system, the responses of the other axes (e.g. lateral, heave, directional) are assumed to be measurement noise. The sources of this measurement noise can include vibration from the motors/propellers, atmospheric turbulence filtered through the plant, and sensor noise. However, frequency sweeps for system identification are conducted in light-to-no wind conditions, so the majority of the off-axis responses can be assumed to come from vibrations and sensor noise and is representative of the measurement noise levels in maneuvering flight.

Figure 11 shows the output autospectra of the pitch and roll rate flight data from a longitudinal sweep. The output autospectra of the swept pitch rate response, G_{qq}, has significantly more energy than the off-axis roll rate response, G_{pp}. The figure also includes an additional output autospectra, $G_{pp_{ground}}$, processed from a data record of the UAS stationary on the ground without turning rotors that represents the baseline level of sensor noise of the Pixhawk flight computer's gyro. The stationary roll rate sensor noise (approximately 0.5 deg/sec) is significantly lower (by a factor of 10) than those measured in flight (5-10 deg/sec seen in Figure 12). This also shows that the majority of the roll rate measurement noise from flight data comes from other sources (e.g. vibration, light turbulence).

From (Ref. 18), the noise output spectrum (G_{nn}) can be calculated from the output autospectrum (G_{yy}), and coherence function (γ_{xy}) between the output y and mixer input x.

$$G_{nn}(f) = [1 - \gamma_{xy}^2(f)]G_{yy}(f) \tag{24}$$

For example, during a pitch sweep, the roll rate measurement assumed to be noise can be calculated as $G_{nn_p} = [1 - \gamma_{\delta_{lon}p}^2]G_{pp}$.

A second-order filter, $N(f)$, is then identified from Eq. 25 such that when white noise of unity power is passed through it, the output is appropriate colored noise that is comparable to that measured from flight test data.

$$G_{nn}(f) = |N(f)|^2 G_{ww}(f) \tag{25}$$

The output of the coloring filter is compared against flight test data for roll rate in Fig. 12. The root-mean-square error (RMSE) between the simulated noise and flight data was 4.5% indicating that the model is producing noise magnitudes similar to that of flight data. It should be noted that the lines are not expected to perfectly match due to the stochastic nature of noise but rather as a qualitative comparison of the frequency content and magnitude.

Case Study Results

A case study was performed by commanding the three FCS to track the mission path shown in Figure 10 using the nonlinear, continuous, full-flight envelope stitched model and disturbances in the form of measurement noise simulated throughout the flight path and turbulence from CETI models in the hover/low-speed portions of the mission. The cases provide a reference for the:

1. Baseline performance by using the unloaded configuration for which the FCS were optimized
2. Degraded performance of each FCS by using the loaded bare-airframe mass properties but without reconfiguration
3. Performance regained through deterministic reconfiguration of the FCS for the known payload

The flight control systems are evaluated based on their ability to maintain tracking of the package delivery route. The 3σ position (x, y, z) tracking error, ε, is computed using Eqn. 26.

$$\varepsilon = 3\sqrt{\frac{1}{n}\sum_{i=1}^{n}((x_{c_i} - x_{m_i})^2 + (y_{c_i} - y_{m_i})^2 + (z_{c_i} - z_{m_i})^2)} \tag{26}$$

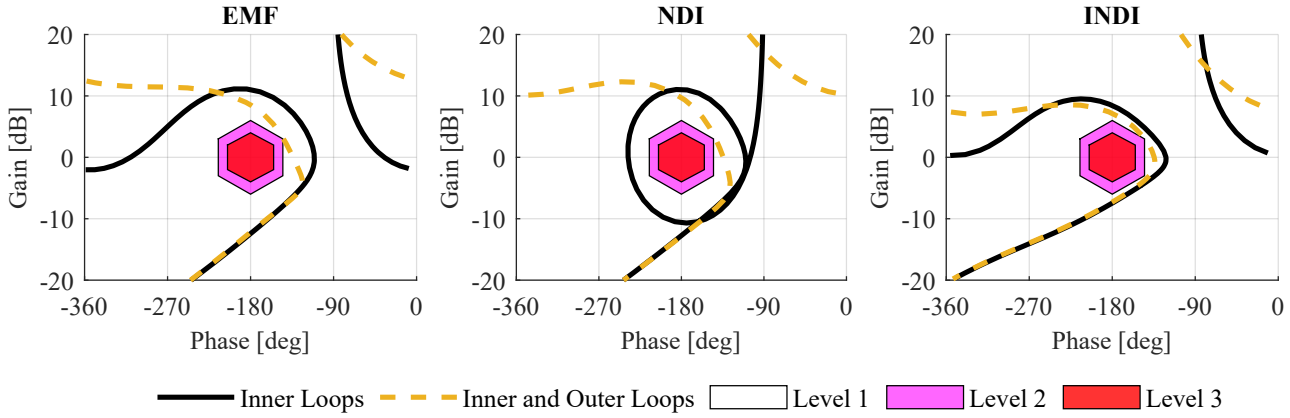

Figure 9: Nichols plot of broken-loop responses at the input to the actuator (lateral axis, hover flight condition).

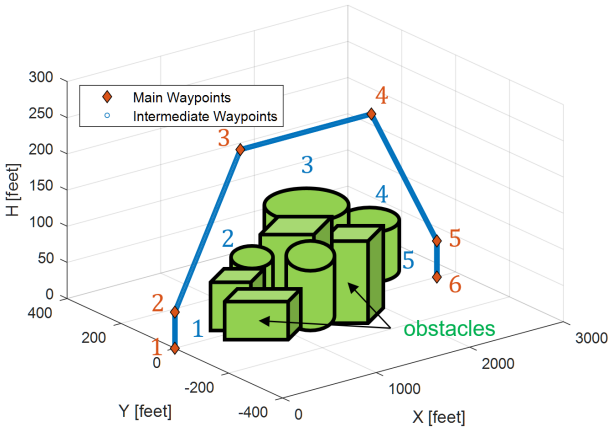

Figure 10: Nominal package delivery mission flight path.

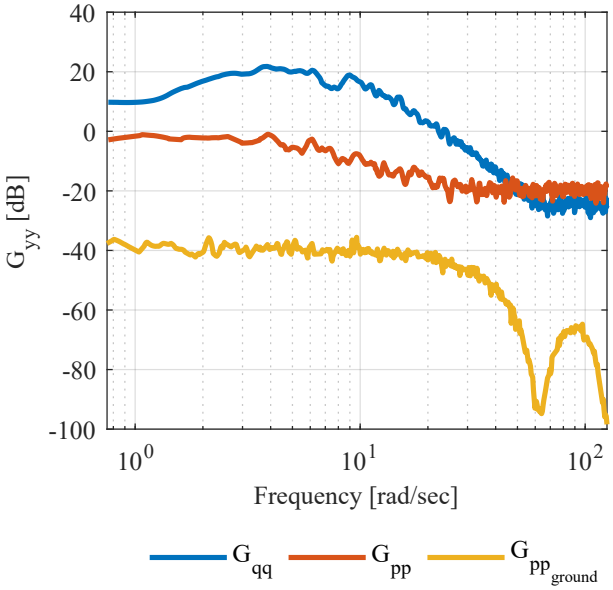

Figure 11: Output autospectra of pitch, roll, yaw, and altitude-rate signals from a longitudinal sweep.

where n=150 for the number of intermediate waypoints in a given path. Figure 13 shows the total tracking error across the entire mission envelope for the three control systems.

Case 1 provided a baseline on the expected performance of the optimized control systems. The trends of each FCS tracked those seen in linear analysis (Figure 8), but were slightly degraded due to the linear interpolation of the feedback gains and varying stitched model dynamics with airspeed.

For Case 2, the stitched model's mass properties were changed to reflect those of the loaded configuration. Without reconfiguration of the flight control system, substantial (on the order of 100%) increase in tracking error was observed for EMF and NDI. The INDI FCS did not have as severe tracking performance degradation without reconfiguration.

In Case 3, the EMF control system was reconfigured by updating the inverse model parameters and computing the cross-feed matrix (Eq. 23) which resulted in nearly identical performance to the nominal case. Likewise, the onboard models of NDI and INDI flight control systems were reconfigured with the extrapolated model of the loaded configuration, the performance greatly improved and nearly returning to the tracking performance of Case 1.

There was a slight decrease in tracking error in paths 1 and 5 (Figure 10) in Case 3 when compared to Case 1. This is due to the fact that simulated turbulence from CETI models produce the majority of the tracking error during these paths since off-axis coupling has been canceled through reconfiguration. Once the mass properties of the stitched model have been updated to reflect the heavy configuration, the same amount of turbulence generated by the CETI models end up having less of an effect on an aircraft with more mass and inertia.

Overall, the EMF control system performed the best in terms of tracking performance in Cases 1 and 3 while having similar performance as the INDI control system without reconfiguration.

ROBUSTNESS ANALYSIS

A comprehensive uncertainty analysis was performed using 500 Monte Carlo simulations. Parametric uncertainties from both the package mass properties as well as modeling uncertainty were considered. Only the lateral axis robustness results at the hover flight condition are presented here for brevity,

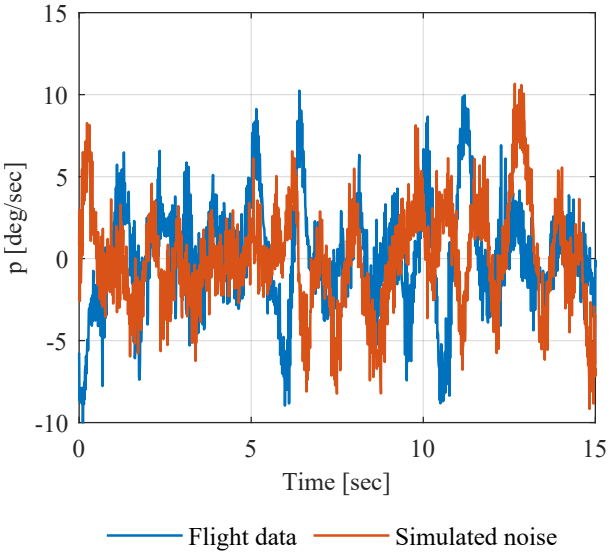

Figure 12: Time domain validation of measurement noise model against flight test data.

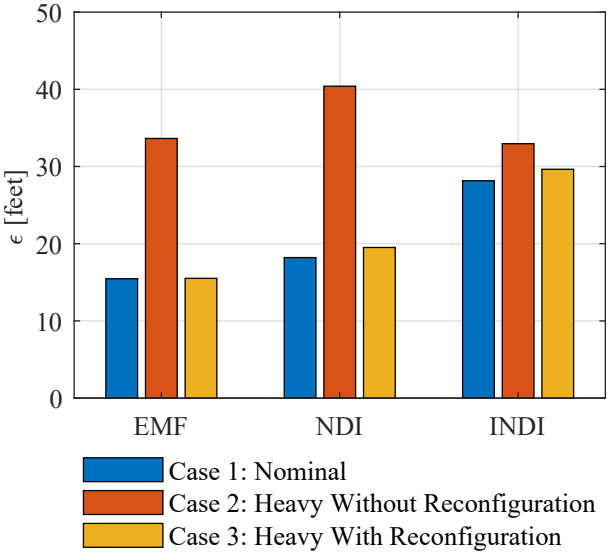

Figure 13: Total tracking error over the course of the mission.

however, the other axes were examined and showed similar trends.

Performance Robustness

Figure 14 shows the closed-loop, lateral axis, inner-loop tracking response ($\frac{\phi_m}{\delta_{lat_p}}$) with and without reconfiguration. For reference, the commanded response, $\frac{\phi_{cmd}}{\delta_{lat_p}}$ (Eq. 1), is shown in black and the nominal response optimized without uncertainties is shown in yellow. The nominal response tracks the commanded response well below 20 rad/sec. Above 20 rad/sec, the low-pass filter seen in Figure 6 set at 50 rad/sec causes the nominal response to additionally "roll-off" to attenuate noise. Figure 14a shows that while the nominal tracking responses of each flight control system is without steady-state error, uncertainties will cause the response to deviate from the command below 1 rad/sec for EMF and NDI. INDI shows no such deviations below 1 rad/sec and maintains excellent tracking without reconfiguration highlighting its performance robustness - an advantage of its architectural design when compared to NDI. Once reconfigured, Figure 14b shows that all three flight control systems maintain nearly indistinguishable performance when compared to their respective nominal designs (i.e. variations overlay on top of nominal design almost perfectly).

Figure 15 shows the lateral inner-loop attitude sensitivity function (ϕ'/ϕ_d) which is the disturbance rejection response (Ref. 10). Variations to the same uncertainties used in evaluation of the command tracking response are shown with and without reconfiguration. The nominal response is shown along with the variations. Each variation's DRB frequency (frequency at which the magnitude is -3 dB) is shown with a vertical (green) line. It also shows two reference lines a horizontal black line at -3 dB where the disturbance rejection bandwidth (DRB) frequency is defined and a horizontal red line indicating Level 1/2 boundary of the disturbance rejection peak (DRP) requirement (4.5 dB). The shape and variations of each flight control system provides insight into the robustness of the disturbance rejection capabilities of each flight controls system. The INDI control system is shown to have the least variation and the best attenuation of disturbances among the three FCS at low frequency at the expense of some cases that exceed the DRP requirement. In comparison, although all cases still meet the DRP requirement, the NDI control system has significantly more variation due to the same uncertainties. Lastly, the EMF control system's disturbance rejection response loop shape does not nearly attenuate disturbances as well at low frequency. As opposed to the NDI and INDI control systems which cancel out the bare-airframe dynamics through feedback linearization, the EMF control system is not able to shape the response as freely due to the unstable bare-airframe dynamics.

Figure 15a shows that each flight control system has a different amount of variation to uncertainty without reconfiguration. INDI is highly robust in disturbance rejection even without reconfiguration as seen by the relatively close tracking of the variations to the nominal response which is consistent with the results seen in the closed-loop tracking performance. However, INDI does have variations that exceed the 4.5 dB Level 1/2 boundary for DRP without reconfiguration. The EMF and NDI control systems have a wider range of DRB variations (seen by the numerous vertical green lines) as compared to INDI, but all variations stay below the DRP requirement even without reconfiguration.

Figure 15b shows that with reconfiguration, variations to the nominal response are suppressed (i.e. blues lines collapse to the yellow dashed line) above the DRB frequency. Reconfiguration allowed all variations of INDI to stay within Level 1 DRP. NDI received the most benefit from reconfiguration as the large number of variations condensed down much closer towards the nominal. The EMF control system did not benefit as much as the NDI control system from reconfiguration

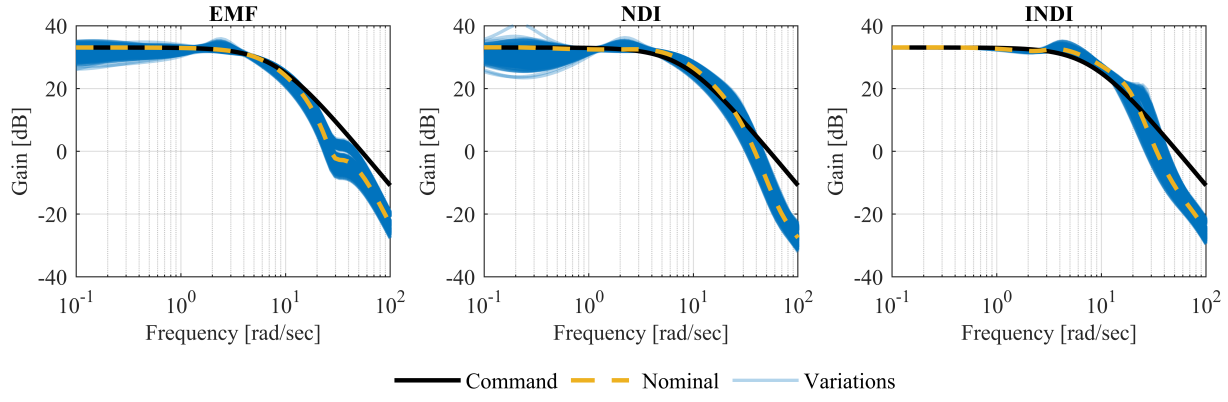

(a) Without reconfiguration.

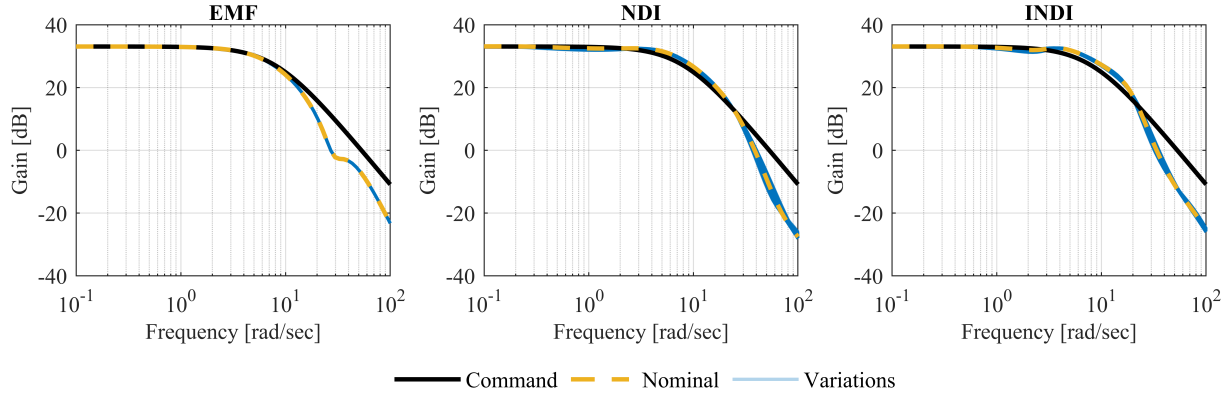

(b) With reconfiguration.

Figure 14: Inner-loop lateral response to uncertainties with and without reconfiguration.

with most improvements to the nominal response occuring after 5 rad/sec. The method of reconfiguration for EMF (cross-feed matrix and inverse model parameter update) are intended to cancel offset CG effects and improve feed-forward command tracking, so the benefits of EMF reconfiguration are not seen at lower frequencies. In general, reconfiguration strategies presented here appear to have less of an effect at lower frequencies in terms of disturbance rejection response.

However, differences in inner-loop attitude disturbance rejection response loop shapes are less significant with the closure of the outer feedback loops. Figure 16 shows that once the outer-loops are closed, the position disturbance rejection responses which dictate how well they aircraft is able to hold its position in the presence of disturbances, are not significantly different. In fact, the INDI control system's position disturbance rejection response has less attenuation at low frequency than the EMF and NDI control systems. Figure 16a shows that the EMF and NDI outer-loop disturbance rejection responses exceed the DRP requirement without reconfiguration. Figure 16b shows that the variations once again collapse towards the nominal design and all variations meet the DRP requirement once the control systems have been reconfigured.

Stability Robustness

Figure 17 shows the variations in the lateral axis broken-loop gain and phase at the input to the actuator after closure of both inner and outer loops. It shows that the gain can only be increased or decreased by a limited amount before reaching instability since the broken-loop responses of all three FCS cross above and below the exclusion zone.

Figure 17a shows the variations in each control system's broken-loop response to uncertainties without reconfiguration. It also shows the response for the loaded configuration that was flight tested for reference. Under uncertainty analysis, SAE-AS94900 specifies that stability margins are allowed to degrade to half of the normal requirement (Ref. 10). It shows that without reconfiguration, EMF and NDI will have variations that cross into the Level 2 region of the exclusion zone but would still satisfy the SAE requirement. However, INDI has larger degradations when the same uncertainties are considered with a large number of cases failing to meet the 50% degraded margins requirement.

Figure 17b shows the effect of reconfiguration on the broken-loop responses. It shows that the variations effectively collapse back to the nominally designed response for all three FCS within the frequencies near the exclusion zone. At very low and high frequencies, the variations still deviate from the nominal response, but those variations do not threaten stability since they are far away from the exclusion zone. This shows that deterministic reconfiguration is able to greatly improve the stability robustness and reliably recover the desirable properties of each flight control system's respective nom-

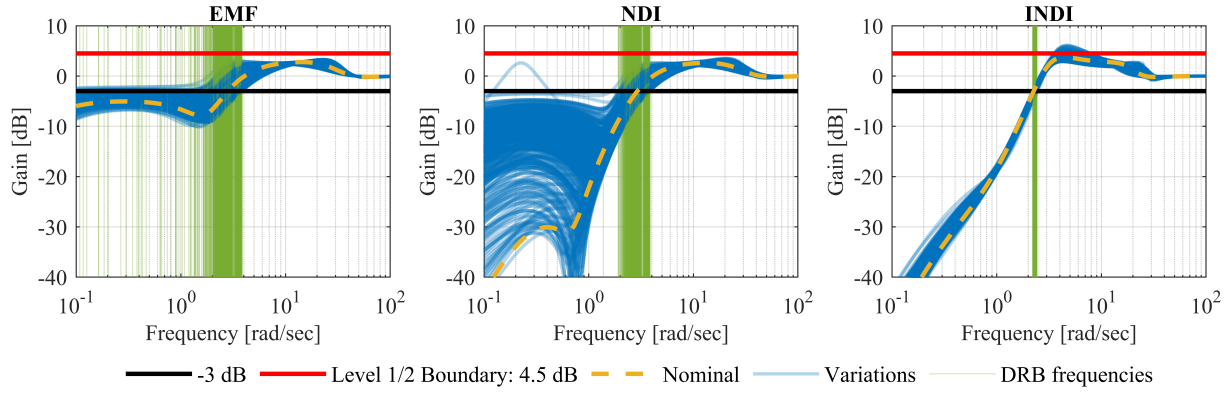

(a) Without reconfiguration.

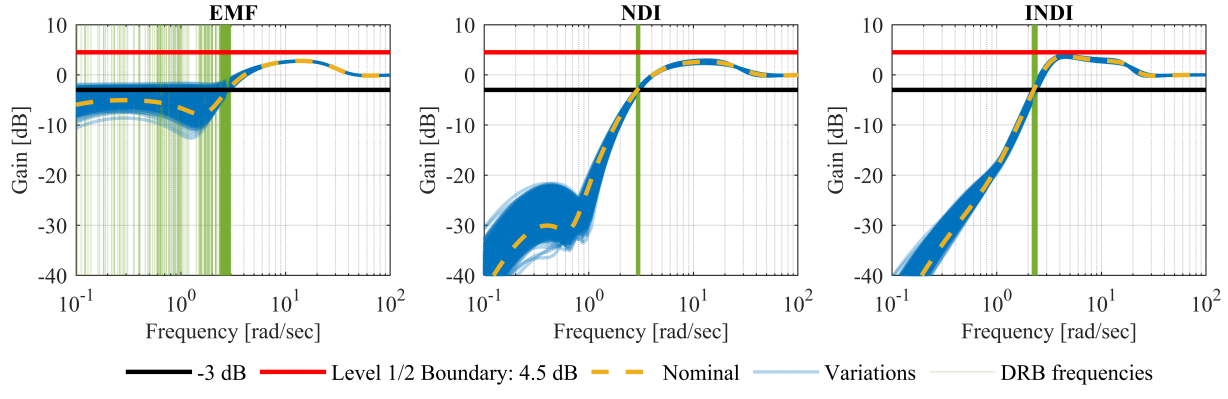

(b) With reconfiguration.

Figure 15: Lateral axis inner-loop attitude sensitivity function variations to uncertainty with and without reconfiguration.

inal design.

DISCUSSION

Practical Considerations of Dynamic Inversion

The ideal case of feedback linearization perfectly cancels the bare-airframe dynamics, rendering the virtual plant an integrator. In a more realistic case, non-instantaneous actuators, time delays, and filter dynamics produce a virtual plant that is not a pure integrator.

Figure 18 shows the virtual plant resulting from feedback linearization using INDI for both the ideal and realistic cases at hover for the roll axis. Referencing Figure 5c, the ideal case considers only a fast actuator model whereas the realistic case includes the identified actuator model (Eq. 21), low-pass filter (Eq. 22), and an additional 21.4 milliseconds of input time delay obtained from system identification. A frequency sweep is used to validate the accuracy of the realistic case that is generated using numerical linearization. The loops are broken at ν, a frequency sweep in summed into the lateral axis channel, and the measured roll rate is used as the output. The simulated frequency sweep time history is processed using the CIFER® software (Ref. 9). Figure 18 shows that the frequency sweep of the realistic case perfectly tracks the result from numerical linearization which provides confidence in using numerical linearization for analyses moving forward. For reference, the figure also includes the on-axis lateral mixer to roll rate bare-airframe response ($\frac{p}{\delta_{lat_c}}(s)$).

Equation 27 shows the bare-airframe roll rate response to lateral mixer input transfer function. For the lateral and longitudinal (not shown) axes, the hover dynamics are second-over-third order transfer functions where the roll mode (T_r) and low-frequency unstable lateral phugoid mode ($[\zeta_{ph},\ \omega_{ph}]$) together make up the "hovering cubic."

$$\begin{aligned}\frac{p}{\delta_{lat_c}}(s) &= \frac{L_{\delta_{lat}}\ s\ (s-Y_v)}{(s+1/T_r)[\zeta_{ph},\ \omega_{ph}]} \\ &= \frac{2886\ s\ (s+0.261)}{(s+2.233)[-0.47,\ 2.098]}\end{aligned} \tag{27}$$

In the ideal case, the unstable bare-airframe dynamics seen in Eq. 27 are perfectly canceled, and feedback linearization produces an integrator from the perspective of the virtual control (i.e. $\frac{p}{\dot{p}_{cmd}}(s) = \frac{1}{s}$) as shown in Figure 18. However, for the realistic case, the resulting virtual plant (Eq. 28) are distorted from the integrator at both low and high frequency. At low frequency, the virtual plant has steady-state gain of -11 dB and a stable, but lightly damped (ζ = 0.11), mode at 0.96 rad/sec. At higher frequency, the virtual plant has a well-damped mode at 31 rad/sec caused by the actuator. The same distortion of the virtual plant from the ideal integrator due to realistic actuators and time delays is also evident in the longitudinal axes

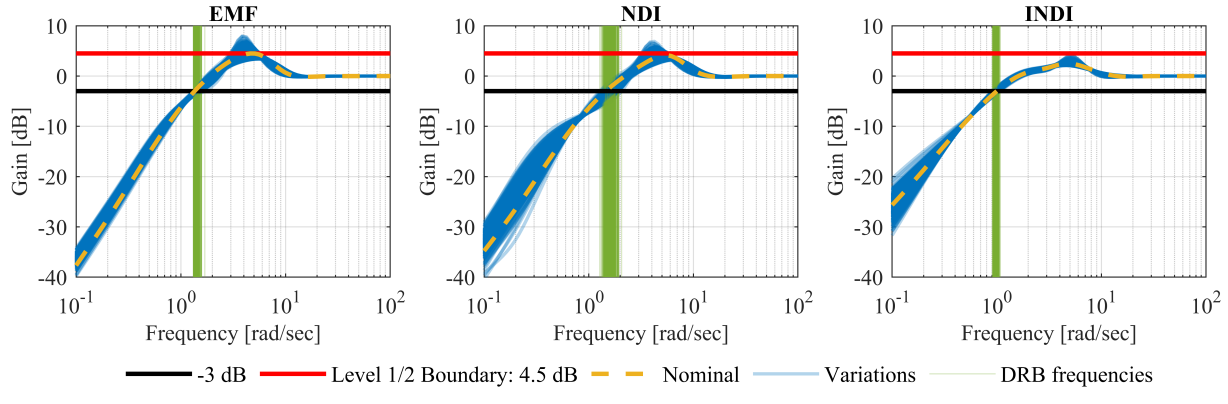

(a) Without reconfiguration.

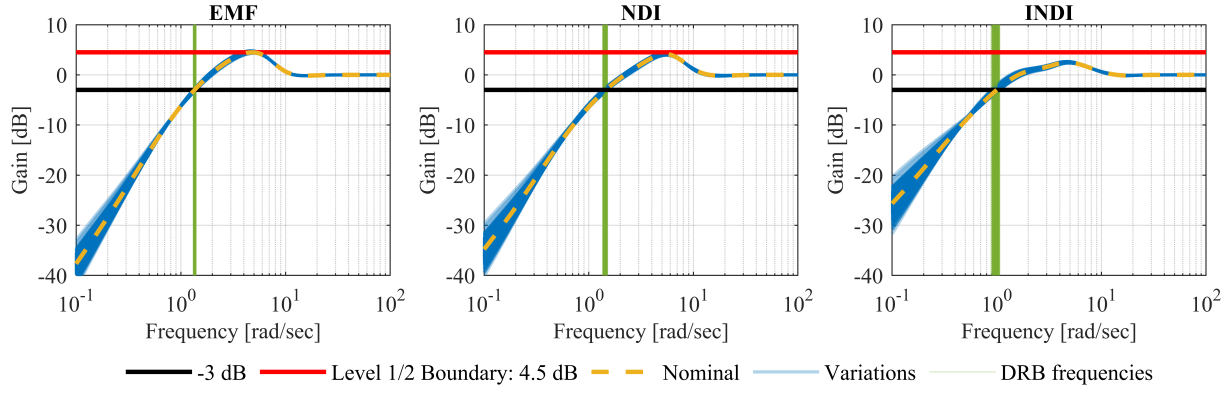

(b) With reconfiguration.

Figure 16: Y-axis outer-loop position sensitivity function variations to uncertainty with and without reconfiguration.

due to symmetry. Though this is shown for INDI, NDI also produces a similarly distorted virtual plant in the lateral and longitudinal axes.

$$\frac{p}{\dot{p}_{cmd}}(s) = \frac{962\ (s+0.261)}{[0.11,\ 0.961][0.92,\ 31.05]} \tag{28}$$

In the ideal case, feedback linearization techniques (e.g. NDI, INDI) will cancel the bare-airframe dynamics and simplify the design of feedback gains. The bare-airframe dynamics which vary throughout the flight envelope can effectively be turned into a simple integrator and therefore, a single set of feedback gains could in theory be sufficient to control the vehicle across the entire flight envelope. This means that scheduling feedback gains with airspeed will not be required since the "scheduling" is done through lookup tables for the onboard models. However, as shown earlier, a realistic case where the assumptions (instantaneous actuators, no time delays) are not valid, the resulting virtual plant will not be an integrator and will also vary with flight condition. This then motivates feedback gains to be be optimized per flight condition to maximize performance. This is significant since NDI and INDI will also require design, optimization, and gain-scheduling of feedback gains with airspeed to maximize performance as opposed to a single set of feedback gains.

Deterministic Reconfiguration Implementation

The stitched model of this aircraft was a key enabling technology for deterministic reconfiguration due to its ability to accurately extrapolate for off-nominally loaded configurations (i.e. those with an internal payload). All three architectures relied on accurate linear models of the loaded configurations to populate lookup tables for reconfiguration of their respective onboard models (inverse models parameters for EMF, $\boldsymbol{F(x)}$ and $\boldsymbol{G(x)}$ for NDI, and the $\boldsymbol{G(x)}$ for INDI).

The main advantage of a linear architecture like EMF when compared to the other two nonlinear control systems is the simplicity and transparency of the designs. The EMF control system's reconfiguration strategy was simple, yet effective, at canceling heave coupling due to offset CG with a simple cross-feed matrix. In was also straightforward to create lookup tables of onboard inverse models parameters. Since NDI and INDI utilize the onboard models in the inner-loop feedback paths for feedback linearization, uncertainties in those models can affect the stability whereas inverse models used in EMF are *not* within the inner-loop's feedback path. The lower-order nature of the inverse models used in EMF also leads to quicker setup of the architecture itself whereas the NDI control system was much more complex due to the need of incorporating the nonlinear equations of motion into $\boldsymbol{F(x)}$.

The EMF flight control system was also the most transparent

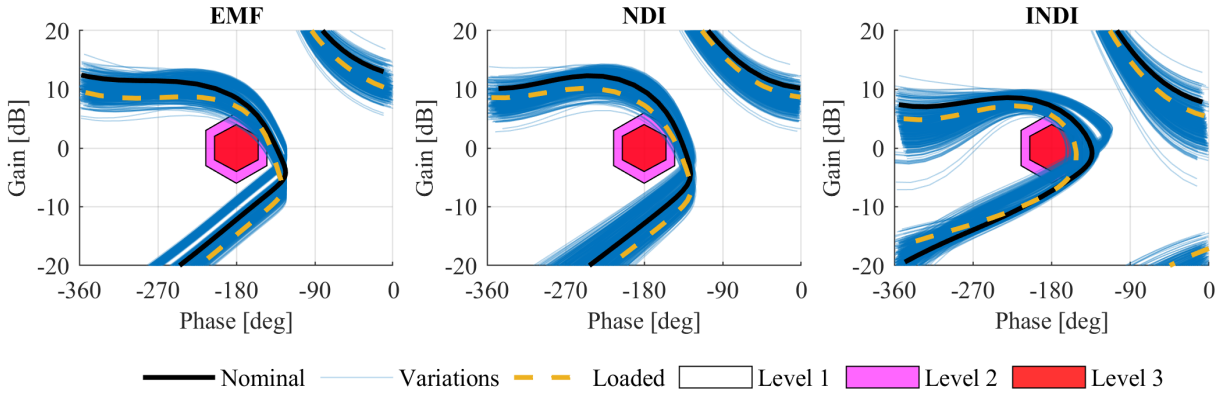

(a) Without reconfiguration.

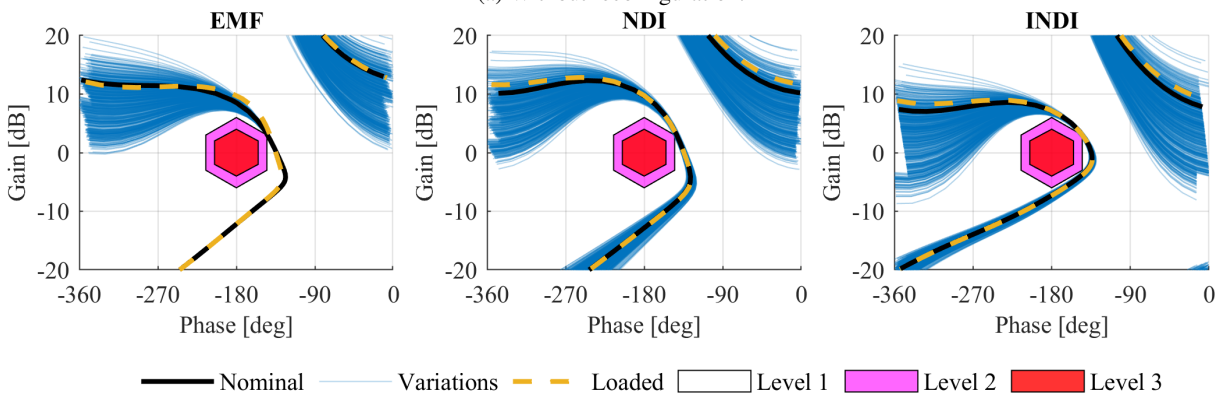

(b) With reconfiguration.

Figure 17: Lateral axis Nichols margin with loop broken at the actuators with and without reconfiguration.

in terms of implementation in conjunction with the full-flight envelop stitched model and the scheduling and interpolation of feedback gains with airspeed. Performance of the EMF control system in nonlinear simulation closely matched results from linear analysis. The theoretical benefits of NDI and INDI using a single set of feedback gains for simplicity were not realized due to non-ideal virtual plants that resulted from slower actuator dynamics and time delays. The feedback gains for the NDI and INDI control systems needed to be scheduled for maximum performance, and as a result, added an additional layer of complexity to their implementation. The added complexity of NDI and INDI did not provide improvements to tracking performance over EMF for the sample mission scenario.

CONCLUSIONS

1. Reconfiguration for payload is necessary to prevent excessive degradation in performance, stability, and undesirable coupling between the thrust and pitch/roll axes.

2. Robustness analysis demonstrated that EMF and NDI flight control systems require reconfiguration to maintain good tracking performance. The INDI flight control system has robust performance in command tracking and disturbance rejection, but will suffer significant stability degradation without reconfiguration.

3. The stitched model is a key technology that enables deterministic reconfiguration strategies by extrapolating for loaded configurations. It allowed for the flight control systems to nearly recover tracking performance comparable to the baseline unloaded configuration.

4. Feedback linearization strategies (i.e. NDI and INDI) that consider realistic time delays and actuator dynamics for package delivery multirotor UAS do not result in the idealized integrator virtual plant on the lateral and longitudinal axes. The deviation from a constant integrator throughout the flight envelope necessitates feedback gains to be designed per flight condition, rather than a singular gain set for the entire flight envelope, for maximum performance.

5. Based on the full-flight envelope nonlinear simulation, the EMF control system performed the best (least tracking error) out of the three architectures for the nominal and reconfigured cases. For the case without reconfiguration, EMF had comparable performance to the INDI control system.

REFERENCES

1. Fan, F., Lin, M., Ding, R., Zheng, Z., and Liu, Y., "Augmented-MRAC for quadrotor UAVs with parameter change," 2016 IEEE International Conference on

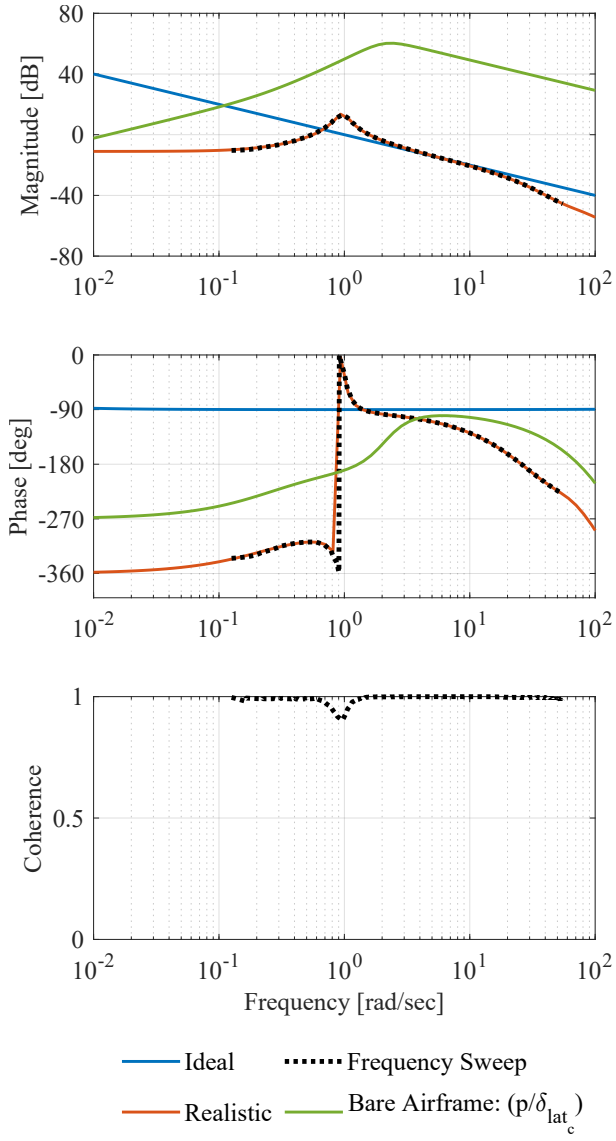

Figure 18: Lateral axis virtual plant ($p/\dot{p}_{cmd}$) from INDI feedback linearization.

Advanced Intelligent Mechatronics (AIM), July 2016. DOI: 10.1109/AIM.2016.7576817

2. Sadeghzadeh, I., Mehta, A., and Zhang, Y., "Fault/Damage Tolerant Control of a Quadrotor Helicopter UAV using Model Reference Adaptive Control and Gain- Scheduled PID," , 2011.

3. Smeur, E., de Croon, G., and Chu, Q., "Cascaded incremental nonlinear dynamic inversion for MAV disturbance rejection," *Control Engineering Practice*, Vol. 73, 2018, pp. 79–90. DOI: https://doi.org/10.1016/j.conengprac.2018.01.003

4. Smeur, E. J. J., Chu, Q., and de Croon, G. C. H. E., "Adaptive Incremental Nonlinear Dynamic Inversion for Attitude Control of Micro Air Vehicles," *Journal of Guidance, Control, and Dynamics*, Vol. 39, (3), Dec 2015, pp. 450–461. DOI: 10.2514/1.G001490

5. Poksawat, P., Wang, L., and Mohamed, A., "Gain Scheduled Attitude Control of Fixed-Wing UAV With Automatic Controller Tuning," *IEEE Transactions on Control Systems Technology*, Vol. 26, 2018, pp. 1192–1203.

6. Gong, A., *Deterministic Reconfiguration of Flight Control Systems for Multirotor UAV Package Delivery*, Ph.D. thesis, University of California - Davis, Dec 2020.

7. Tobias, E. L., and Tischler, M. B., "A Model Stitching Architecture for Continuous Full Flight-Envelope Simulation of Fixed-Wing Aircraft and Rotorcraft from Discrete-Point Linear Models," U.S. Army AMRDEC Special Report RDMR-AF-16-01, April 2016.

8. Gong, A., Sanders, F. C., Hess, R. A., and Tischler, M. B., "System Identification and Full Flight-Envelope Model Stitching of a Package-Delivery Octocopter," AIAA Atmospheric Flight Mechanics Conference, Jan 2019. DOI: 10.2514/6.2019-1076

9. Tischler, M. B., and Remple, R. K., *Aircraft and Rotorcraft System Identification: Engineering Methods and Flight Test Examples Second Edition*, AIAA education series, American Institute of Aeronautics and Astronautics, Aug 2012. DOI: 10.2514/4.861352

10. Tischler, M. B., Berger, T., Ivler, C. M., Mansur, M. H., Cheung, K. K., and Soong, J. Y., *Practical Methods for Aircraft and Rotorcraft Flight Control Design: An Optimization-based Approach*, AIAA education series, American Institute of Aeronautics and Astronautics, 2017.

11. Stevens, B., and Lewis, F., *Aircraft Control and Simulation*, Wiley, 2003.

12. Smith, P., "A simplified approach to nonlinear dynamic inversion based flight control," 23rd Atmospheric Flight Mechanics Conference. DOI: 10.2514/6.1998-4461

13. Berger, T., Tischler, M. B., Hagerott, S. G., Cotting, M. C., Gray, W. R., Gresham, J., George, J., Krogh, K., D'Argenio, A., and Howland, J., "Development and Validation of a Flight-Identified Full-Envelope Business Jet Simulation Model Using a Stitching Architecture," AIAA Modeling and Simulation Technologies Conference, Jan 2017.

14. Lopez, M. J. S., Tischler, M. B., Soong, J. Y., Nadell, S. J., Sanders, F. C., and Gong, A., "Flight Test Comparison of Gust Rejection Capability for Various Multirotor Configurations," Vertical Flight Society 75th Annual Forum, May 2019.

15. Tischler, M. B., Blanken, C. L., Cheung, K. K., Swei, S. S. M., Sahasrabudhe, V., and Faynberg, A., "Modernized Control Laws for UH-60 BLACK HAWK Optimization and Flight-Test Results," *Journal of Guidance, Control, and Dynamics*, Vol. 28, (5), 2005, pp. 964–978. DOI: 10.2514/1.8021

16. Berrios, M., Berger, T., Tischler, M., Juhasz, O., and C Sanders, F., "Hover Flight Control Design for UAS Using Performance-based Disturbance Rejection Requirements," American Helicopter Society 73rd Annual Forum, May 2017.

17. Harris, J. J., and Stanford, J. R., *F-35 Flight Control Law Design, Development, and Verification*, 2019, pp. 287–311. DOI: 10.2514/5.9781624105678.0287.0312

18. Bendat, J., and Piersol, A., *Random Data: Analysis and Measurement Procedures*, Wiley Series in Probability and Statistics, Wiley, 2011.